1
2

The Martian bow shock over solar cycle 23-24 as observed by the Mars Express mission

3

4

B. E. S. Hall[1], B. Sánchez-Cano[2], J. A. Wild[1], M. Lester[2], M. Holmstrom[3]

5

6 [1] Physics Department, Lancaster University, Lancaster, UK.

7 [2] Physics and Astronomy Department, University of Leicester, Leicester, UK.

8 [3] IRF Kiruna, Kiruna, Sweden.

9

10 **Corresponding author:** B. Sánchez-Cano   bscmdr1@leicester.ac.uk

11 **Key points**

12   1. Between the solar minimum and maximum phases of cycle 23-24, the average
13   Martian bow shock distance increases by 7%
14   2. The bow shock surface is modeled from Mars Express observations over the
15   period of 2004-2017
16   3. Bow shock position and solar EUV flux vary similarly over the solar cycle and
17   Martian year

18

19 **Key words**

20 Mars, Bow Shock, Solar Cycle, Mars Express, ASPERA-3, Solar EUV

21 **Index terms**

22 2154, 2162, 2780, 6225, 6026

23

24

25 **Abstract**

26 The Martian bow shock position is known to be correlated with solar extreme ultraviolet

27 (EUV) irradiance. Since this parameter is also correlated with the evolution of the solar

28 cycle, it is expected the Martian bow shock position should also vary over such a period.

29 However, previous reports on this topic have often proved contradictory. Using 13 years

30 of observations of the Martian bow shock by the Mars Express mission over the period

31 2004 to 2017, we report that the Martian bow shock position does vary over the solar

32 cycle. Over this period our analysis shows the bow shock position to increase on average

33 by 7% between the solar minimum and maximum phases of solar cycle 23-24, which

34 could be even larger for more extreme previous solar cycles. We show that both annual

35 and solar cycle variations play major roles in the location of the bow shock at Mars.

36

37 **Plain language summary**

38 The solar wind, which is material ejected by the Sun, interacts directly with the upper

39 atmosphere of Mars and its plasma environment. This interaction region is enclosed by a

40 bow shock, a boundary where the solar wind is rapidly slowed so it can be diverted

41 around the Martian space environment. The Sun's solar activity, the behavior of its

42 material and light output over time, varies over many different periods, resulting in a very

43 dynamic Martian space environment. Studies of how the solar cycle, a ~11 year variation

44 in the solar activity, impacts the Martian space environment has been inhibited by a lack

45 of continuous observations of the environment. However, the European Space Agency's

46 Mars Express mission has surveyed the Martian environment for >11 years. We use the

47 longevity of this mission to describe how the Martian bow shock varies over this long

48 period for the first time. In contrary to previous time-limited studies, we show that the

49 Martian bow shock position is impacted by the solar activity, moving away from Mars as

50 the solar activity increases. These results are important to future studies and missions

51 that probe the interaction of the Martian atmosphere with the solar wind.

52

53

54

1. Introduction

The Martian bow shock develops to slow the supermagnetosonic flowing solar wind to subsonic speeds such that it can be diverted about the Martian plasma system. Unlike celestial bodies that are enclosed within an intrinsic global magnetic field (e.g., the magnetosphere of Earth), Mars' ionosphere and extended exosphere instead acts as an obstacle to the solar wind flow. In this sense, Mars and Venus are very similar planets, sharing an ionosphere as well as an exosphere extending outside the bow shock and so, contributing to the obstacle to the solar wind plasma flow.

The location of the bow shock depends on several drivers that can be either external, such as the solar extreme ultraviolet (EUV) flux, the solar cycle phases, the solar wind dynamic pressure, the interplanetary magnetic field (IMF) orientation, or the magnetosonic Mach number; or internal, such as the crustal magnetic field sources location rotating with the planet. Both types of drivers produce different types of bow shock variability, which can manifest on short and long time-scales. More details can be found in e.g. Mazelle et al. (2004) or Hall et al. (2016).

Focusing on the EUV parameter as a driver, the solar cycle variation is well-known to play a major role in the location of the bow shock at Venus. Alexander and Russell (1985) indicated that this behavior was caused by neutral atmosphere variations with the solar cycle and its consequent effect on the mass-loading of the solar wind. However, solar cycle variations in the Martian bow shock location have yielded contradictory results to date. The reason could be the different relative distances to the Sun, as previous missions made measurements at different radial distances and levels of solar EUV flux.

Despite the large number of missions exploring Mars in the last 50 years, only Mars Express (MEX) has, so far, measured the solar wind-Mars interaction continuously over a full solar cycle. Before MEX, the Martian bow shock was partially sampled by various spacecraft since the 1960s, as summarized in Table 1. This includes the flyby of Mars by Mariner-4 in 1965 (e.g., Smith et al., 1965; Dryer and Heckman, 1967; Smith, 1969); the Mars-2,3 (December 1971 - March 1972, e.g., Dolginov et al., 1973; Marov and Petrov, 1973), and Mars-5 orbiters (February 1974, e.g., Dolginov et al., 1976; Russell, 1977; 1980; Slavin and Holzer, 1982); the Phobos-2 orbiter (January - March 1989, e.g., Riedler et al., 1989; Slavin et al., 1991; Dolginov and Zhuzgov, 1991; Russell et al., 1992); and the

86 Mars Global Surveyor (MGS) orbiter during its aerobraking phase (1997 - 1999, e.g.,
87 Albee et al., 1998; Vignes et al., 2000; 2002). While these missions have observed the
88 Martian bow shock, the measurements have been sparsely distributed over different
89 seasons and levels of solar activity, as well as spanning separate solar cycles (see Table
90 1).

91 Recent studies have found that the bow shock position at Mars is sensitive to EUV
92 radiation (e.g., Edberg et al., 2009b; Hall et al., 2016; Halekas et al., 2017; Gruesbeck et al.,
93 2018). Therefore, we may initially expect some form of solar cycle period variability in
94 the average bow shock position. Solar cycle studies of the Martian bow shock have been
95 attempted by comparing the observations of bow shock location by the variety of the
96 older missions (see a summary in Table 2). The Mariner-4 (pre-maximum phase of cycle
97 20) and Mars-2,3,5 (post-maximum phase of cycle 20) missions recorded a total of 24
98 bow shock crossings which occurred during a period of moderate solar activity with an
99 average sun spot number, SSN, of 59 (Slavin et al., 1991). The Phobos-2 mission recorded
100 up to 126 bow shock crossings (e.g., Trotignon et al., 1993), 94 reported by Slavin et al.
101 (1991) occurring during a period of higher solar activity (near the maximum phase of
102 cycle 22) with an average SSN of 141 (Slavin et al., 1991). By comparing statistically
103 computed model shock surfaces of the observations at each phase of the solar cycle,
104 Slavin et al., (1991) reported no apparent solar cycle variation in the bow shock position.
105 Modolo et al. (2006) reported a similar finding based on hybrid simulations at the
106 maximum and minimum of solar activity. However, using very similar datasets and
107 methods, Russell et al., (1992) and Trotignon et al., (1993) reported the opposite. Vignes
108 et al., (2000; 2002) extended the previous work by including the 450 bow shock crossings
109 recorded by the MGS mission. These observations occurred during a period where the
110 SSN ranged between 30 and 90 (pre-maximum phase of cycle 23), and, as with the Slavin
111 et al., (1991) study, Vignes et al., (2000;2002) also reported no obvious solar cycle
112 variability in the Martian bow shock position.

113 In order to determine whether the Martian bow shock position varies with the solar cycle,
114 we require near-continuous observations of the bow shock over a solar cycle period by
115 the same instrumentation. The MEX mission (Chicarro et al., 2004) has been sampling the
116 Martian plasma system since December 2003 in an elliptical (~10,000km apoapsis,
117 ~350km periapsis), 7 hr period orbit that precesses around Mars with time. Moreover,

118 due to the MEX trajectory, the Martian dawn hemisphere at apoapsis altitudes is sampled

119 more than the dusk hemisphere. Therefore, there are much more bow shock crossings

120 over the dawn region. Since this orbit typically results in MEX crossing the Martian bow

121 shock several times a day, and MEX carries appropriate plasma instrumentation to detect

122 this boundary, it is the appropriate mission for studying the entire solar cycle variability

123 of this aspect of the Martian plasma system.

124 The objective of this paper is to assess for the first time with the same dataset how the

125 Martian bow shock varies across the solar cycle, and to what extent. This is an important

126 question because we know that the Martian plasma system reacts differently for similar

127 levels of EUV-flux at different phases of the solar cycle (e.g. Sánchez-Cano et al., 2015;

128 2016; 2018). We present an investigation using the entire MEX dataset, and present an

129 analysis of the bow shock position in relation to annual EUV variations, as well as

130 different solar activity phases of the solar cycle. We do not focus on the dynamic pressure

131 parameter because using the same dataset of this study, Hall et al. (2016) recently

132 reported that the bow shock location is more sensitive to variations in the solar EUV

133 irradiance than to solar wind dynamic pressure variations.

134 The remainder of this paper will detail the datasets and methods used (Section 2) to

135 determine whether or not the Martian bow shock position does vary over the period of

136 solar cycle 23-24 (Sections 3-5).

2. Dataset and Analysis

138 The main dataset used in this study originates from the Hall et al. (2016) report on the

139 annual (Martian year) variation in the Martian bow shock position. Hall et al., (2016)

140 devised an automatic algorithm to scan the full (at the time) MEX Analyzer of Space

141 Plasmas and Energetic Atoms Electron Spectrometer (ASPERA-3 ELS, Barabash et al.,

142 2006) dataset for bow shock crossings. Across the period of January 2004 to May 2015,

143 the authors identified 12,091 bow shock crossings. In addition to this Hall et al., (2016)

144 bow shock crossing list, henceforth referred to as the HALL16 dataset, we incorporate

145 additional recently released MEX ASPERA-3 ELS observations to extend the HALL16

146 crossing list to the end of 2017 (and a total of 13,585 crossings). The additional bow shock

147 observations from this extended dataset were extracted using the HALL16 automated

148 identification algorithm. We note that only MEX data has been used in this study in order

149 to avoid wrong-statistical comparisons with datasets from other missions which were
150 not cross-calibrated with respect to MEX observations, such as the crossings shown in
151 Table 2 and the different datasets from the Mars Atmosphere and Volatile EvolutioN
152 (MAVEN) mission. Moreover, all of these missions only cover a small portion of the solar
153 cycle. Therefore, in order to perform a coherent statistical study, only observations from
154 the same dataset are compared.

155 To describe the different phases (or levels of activity) of the Sun over the solar cycle, three
156 supplementary datasets from spacecraft that observe the Sun from 1 AU have been used.
157 (1) The 10.7 cm solar radio flux, $F_{10.7}$, from the OMNI-2 dataset (King and Papitashvili,
158 2005). This index is an excellent indicator of solar activity and it is measured daily at the
159 Penticton Radio Observatory in British Columbia, Canada. (2) The SSN also from the
160 OMNI-2 dataset, which takes the data from the WDC-SILSO, Royal Observatory of
161 Belgium, Brussels. (3) Solar EUV flux, I_{EUV}, measured by the Thermosphere, Ionosphere,
162 Mesosphere Energetics and Dynamics (TIMED) Solar EUV Experiment (SEE) (Woods et
163 al., 1998). The solar EUV flux has also been extrapolated from Earth to Mars to account
164 for the angular and radial separation between the two planets with respect to the solar
165 surface (e.g. Yamauchi et al., 2015, Hall et al., 2016).

166 To study the spatial evolution of the Martian bow shock position over the period of a
167 Martian year, Hall et al., (2016) computed a 2D statistical model of the Martian bow shock
168 surface in an axisymmetric plane (about Sun-oriented axis) of the solar wind aberrated
169 Mars-Centric Solar Orbital (MSO) coordinate system. To study the spatial effects with
170 respect to temporal changes in the bow shock position, the authors then used this model
171 surface to extrapolate each individual crossing to a common reference point, that is, the
172 terminator plane. In this study, we provide a recalculated and more robust model from
173 the entirety of the extended HALL16 crossing dataset such that we can use it to complete
174 the same extrapolation. For the most part, we used the same fitting procedure as the Hall
175 et al., (2016) study, which included:

176   1. Rotating the crossings into the solar wind aberrated MSO system (4° rotation
177   about the Z_{MSO} axis), thus accounting for the average direction of solar wind with
178   respect to Mars' orbital motion.

179   2. Transforming the cartesian aberrated MSO coordinates into polar coordinates as

180   defined by Equations 1 and 2, where r and θ are the polar coordinates of each

181   crossing with respect to a conic's focus located at $(x_0,0,0)$.

182   3. Computing a regression analysis of all crossings with respect to the linearized

183   form of the conic section equation (Equation 3 in form of $r^{-1} \propto cos\theta$), where L is

184   the semilatus rectum, and ϵ is the conic's eccentricity.

$$r = \sqrt{(X'_{MSO} - x_0)^2 + Y'^2_{MSO} + Z'^2_{MSO}} \qquad (1)$$

$$cos\,\theta = \frac{(X'_{MSO} - x_0)}{r} \qquad (2)$$

$$r = \frac{L}{1 + \epsilon\,cos\theta} \qquad (3)$$

185   The Hall et al., (2016) study repeated Steps 2 and 3 of this method for many different x_0

186   parameters, determining the best final set of conic parameters (x_0, L, and ϵ) from the

187   regression results giving the maximum coefficient of determination (i.e., the R^2

188   correlation statistic). Here, we have improved upon the selection of the x_0 parameter by

189   adopting basic machine learning techniques such as train-test and k-fold cross-validation

190   (CV) schema (e.g. Fushiki et al., 2011 and references in there). For each input x_0

191   parameter, this new process adhered to the following procedure:

192   1. Split the full dataset into 10 random subsets, or folds (note: the same random

193   subsets are used for each x_0).

194   2. Select one of the folds as a validation/testing dataset and set aside. Perform

195   regression analysis on the data in the remaining 9 folds (or training subsets). Next,

196   apply resultant model on reserved validation fold to measure its predictive

197   performance (i.e., R^2 statistic).

198   3. Repeat Step 2 until all folds have been used as a training or validation/testing

199   subset, and average the fit statistics of each run to give a performance metric for

200   each input x_0 parameter.

201   The final x_0 fit parameter was chosen from the CV run giving the largest R^2 output. Finally,

202   this optimal x_0 was used in the fitting procedure applied to the full dataset, giving the full

203   set of conic section fit-parameters defined earlier. This CV technique gives a more

204   statistically robust estimate of x_0 than the Hall et al., (2016) method that effectively used

205   a 1-fold CV. Using this more robust fitting procedure, we obtain for the whole dataset

206   (including the new additional crossings, Table 3): x_0=0.760 R_M, L=1.802 R_M, ϵ=0.998 and

207   R_{TD}=2.445 R_M; while Hall et al., (2016) found: x_0=0.740 R_M, L=1.820 R_M, ϵ=1.010 and

208   R_{TD}=2.460 R_M. The new algorithm, therefore, agrees very well with the previous

209   detections with less than a 1% difference.

210   To extrapolate each bow shock crossing to the terminator plane, each set of aberrated

211   MSO coordinates and the final x_0 and ϵ conic fit parameters are substituted into Equations

212   1 to 3 to determine an L parameter for each crossing. All three conic parameters are then

213   substituted into Equation 4 to obtain the extrapolated bow shock terminator distance,

214   R_{TD}.

$$R_{TD} = \sqrt{L^2 + (\epsilon^2 - 1)x_0^2 + 2\epsilon L x_0} \qquad (4)$$

215   This is the same method as used in the Hall et al., (2016) study. In doing this, a proxy for

216   the bow shock positions at a common reference point can be tracked over time.

217   The fit parameters and model terminator distance for the updated bow shock model from

218   the entirety of this study's crossing list, and for the same procedure applied to each

219   Martian year of observations is given in Table 3. The uncertainties given in this table are

220   from the standard error on the fit parameters, and from their consequent use in standard

221   error combination formulae (Hughes and Hase, 2010) for any computed values (e.g.

222   model R_{TD}). These models will be referred to throughout the remainder of the paper.

223   **3. Results**

224   Figure 1 presents time series of the $F_{10.7}$ radio flux (Fig.1a-left ordinate, green), SSN

225   (Fig.1a-right ordinate, purple), TIMED-SEE solar EUV flux extrapolated to Mars (Fig.1b-

226   left ordinate, red) and at Earth (Fig.1b-right ordinate, green), and the extended HALL16

227   extrapolated bow shock terminator distance, R_{TD}, dataset (Fig.1c), all over the period of

228   January 2004 to the end of 2017. This period covers approximately 7 Martian years (MY,

229   687 terrestrial days, see top of panel a), and a full solar cycle of variability, in particular

230 the cycles referred to as solar cycle 23 and 24 (start of cycle 24 denoted at the top of the

231 figure).

232 The $F_{10.7}$, and SSN parameters (Figure 1a) are commonly used proxies for solar activity,

233 and thus the solar cycle. A median filter of temporal box-width 27-days has been applied

234 to both of these parameters to remove the short-term variability associated with the

235 rotation of the solar surface. At the start of MY27 (Feb 2004), the solar activity is declining

236 towards a minimum around mid-MY29, marking the start of cycle 24 around December

237 2008. The activity then increases, peaking near the start of MY32 (Jan 2014), before once

238 again declining in activity by the end of this time series (towards end of MY33).

239 This general trend of solar activity over the solar cycle is clearly reproduced in the solar

240 EUV flux at Earth (Figure 1b-right ordinate, green). At Mars distance, (Figure 1b-left

241 ordinate, red), significant MY-period variations caused by Mars' eccentric orbit of the Sun

242 are clearly visible. Hall et al. (2016) highlighted that this factor drives spatial variations

243 in the average Martian bow shock position over the Martian year. However, we note that

244 despite the MY-period variation, the solar cycle variability is clearly visible in the EUV

245 flux extrapolated to Mars, especially when comparing the EUV flux at same heliocentric

246 distances for different MY (e.g. each EUV minimum and maximum which correspond to

247 farther and closer Mars-Sun positions, respectively).

248 Figure 1c shows each individual crossing extrapolated to the terminator plane (grey

249 dots), and a median filtered (27-day temporal window size) profile (black line) to show

250 its average variability within a solar rotation time period. The blue envelope about this

251 profile represents the median absolute deviation of the extrapolated R_{TD} within each

252 filter box. The absence of a filtered profile at the start of the dataset is due to the limit set

253 which is set on the filtering of least 54 crossings per filter-window, corresponding to a

254 minimum of two bow shock crossings per day. For nominal MEX orbital trajectories, two

255 crossings per orbit are expected, or $\sim$6 crossings per day. We have relaxed our filter-

256 window observation limit from this in order to present as much data as possible, while

257 minimizing spurious filter results. Finally, the median filtered R_{TD} value at each

258 timestamp is calculated from the preceding 27 days of observations.

259 Compared with the median R_{TD} across the entire unfiltered dataset ($\widetilde{R_{TD}} = 2.48\ R_M$,

260 dashed red-line in Figure 1c), we see two periodic variations in the filtered R_{TD} profile

261   (black-line). The first corresponds to the period of a MY and the annual modulation of the

262   EUV flux at Mars (clearest in MY29 and 30), as noted previously by Hall et al., (2016). The

263   second is a longer term trend where the filtered R_{TD} is mostly below $\widetilde{R_{TD}}$ during the solar

264   minimum phase (MY28-30), then mostly above $\widetilde{R_{TD}}$ during the solar maximum phase

265   (MY31-32), before reducing again to around $\widetilde{R_{TD}}$ values as the solar activity declines

266   again around MY33. This longer-term variation is more relatable to the evolution of the

267   solar activity proxies over a period of the solar cycle. Figure 2 highlights both of these

268   variations in more detail, in particular with a focus on quantifying the apparent solar

269   cycle variation.

270   Figure 2a presents the solar EUV flux at Mars (blue), the median-filtered profile of the

271   extended HALL16 with a pass band of 27-days in red to remove the solar rotation period,

272   and the median-filtered profile of the extended HALL16 with a pass band of 687-days in

273   green to remove the variation caused by a Martian year. The three profiles in Figure 2a

274   are on the same ordinate scale. The scale of these parameters are in standardized units

275   (denoted R'_{TD} and I'_{EUV}), where the dataset population mean, μ, is subtracted from each

276   observation before normalizing by the population standard deviation. This scaling allows

277   us to directly compare multiple quantities that have different magnitudes, means, and

278   variances (i.e. in standardized form they both have μ=0 and σ=1). A line at the

279   standardized value of 0 ($R_{TD}-μ(R_{TD})=0σ$) is superimposed to aid description. The MY, a

280   color-coded season (in terms of the solar longitude, L_S, in the key below panel) has also

281   been provided above this panel for more context.

282   The EUV trend and the 27-day filtered R'_{TD} trends clearly vary in almost unison across

283   the period of the solar cycle, although the bow shock total variation between Mars'

284   aphelion and perihelion is larger after 2011 (higher solar activity phase) than before

285   (lower solar activity phase). There is a notable exception at the aphelion of MY32 where

286   the bow shock variability when compared to perihelion is smaller than for other years.

287   Moreover, during the `through perihelion' passages of Mars orbit (red color-coded season

288   sectors), $R'_{TD,27day}$ can peak by a larger amount than the EUV flux (e.g., see MY29 and 30

289   for clear examples). We do not know the origin of this extra variability which seems not

290   related to EUV fluxes, but we note that at that time, there was a notable rise on the soft X-

291   ray background radiation which could explain these larger values from 2011 till mid-

292   2015 (see e.g. Sanchez-Cano et al., 2015; 2016). X-ray fluxes are known to be the

293   ionization source below the main peak of the ionosphere (~130km) (e.g. Mendillo et al.,

294   2006). Therefore, if the X-ray flux is more intense during a particular period, the lower

295   ionosphere is more robust, and can contribute to an enhanced thermal pressure of the

296   ionosphere. Consequently, the Mars' plasma obstacle to the solar wind is enhanced, and

297   the bow shock location could be found further from Mars. The MY R'_{TD} profile (green),

298   also had a minimum observation limit for the filter window set to two observations per

299   day (or 1374 observations per filter window). Consequently, this filtered profile starts

300   later into the dataset during the perihelion sector of MY28. Nevertheless, this filtered

301   profile clearly shows a change from the average bow shock terminator position being

302   around or below -1 standardized units ($R_{TD}-\mu(R_{TD})=-1\sigma$) during solar minimum (MY28

303   and 29, see Figure 1a), before increasing to ~1 standardized units $R_{TD}-\mu(R_{TD})=1\sigma$

304   around solar maximum (MY31 and 32). Moreover, as the solar activity then begins to

305   decrease again (e.g. MY33), this profile starts to decrease back to the average amount of

306   0 standardized units. The $R'_{TD,687day}$ profile (green) clearly shows that despite any other

307   variation caused by Mars' orbit about the Sun, there is a clear solar cycle trend on the bow

308   shock position. This confirms the finding of previous studies such as Trotignon et al.

309   (1993).

310   While the time series shown in Figure 2a shows both clear annual, and solar cycle

311   variations in the Martian bow shock position, to extrapolate each crossing to the

312   terminator plane we have assumed that the model Martian bow shock remains the same

313   across the entire period. To investigate this assumption, a model for the bow shock (using

314   the method outlined earlier) was calculated for each MY of observations across the period

315   (annual average). It was not possible to perform this annual fit for same Sun-Mars

316   distance conditions due to scarce data coverage for all the periods at a same distance. The

317   results of this is shown across Figure 2b-i and in Table 3.

318   Figure 2b-h show the MEX bow shock crossings (grey dots) and model shock surfaces

319   (various colored curves) for each MY in the aberrated cylindrically symmetric MSO

320   coordinate system. The corresponding MY and model terminator distance, $R_{TD,model}$, have

321   been superposed in each panel, and as a time series in Figure 2i. The error bars on each

322   point in panel i (see Table 3) have been doubled for visibility. This panel also shows

323   reference lines at the mean ($\mu=2.43R_M$, solid black) and 1σ ($\sigma=0.06R_M$, dashed black)

324   levels of the $R_{TD,model}$ population.

325 Figure 2b-h shows the variation in the spatial coverage and observation frequency of the
326 Martian bow shock by MEX between each MY. For example, MY27 (panel 2b) had fewer
327 observations than any other period, but were nevertheless well distributed along the
328 shock surface in this reference frame. All other MY's had many more observations (also
329 see Table 3), but sometimes had significant gaps in spatial uniformity about the
330 terminator (e.g., MY29-31, panels 2d-e). Fortunately, such MY's also had significant
331 numbers of observations either side of the terminator, resulting in the fit being well
332 constrained about the terminator, and giving an $R_{TD,model}$ estimate expected to be
333 representative of the period. Figure 2a (and 1c earlier) show that each MY of crossings
334 are not necessarily well distributed throughout all seasons of that year. For example,
335 MY28 and 29 (panel 2b,c) both have reduced crossing frequency during Mars' aphelion
336 passage (aqua color-coded season sector). Conversely, MY28 and 32 have limited
337 numbers of crossings during the perihelion phase (red sector). As reported previously by
338 Hall et al., (2016), the Martian bow shock exhibits a significant variation in average
339 position between these two seasonal sectors. It is due to these above factors that we often
340 opt to use the entire dataset, where all seasonal periods are covered multiple times and
341 the crossings present an equal spatial uniformity along the shock surface, to extrapolate
342 each observations to a common reference point. Despite the spatial and temporal
343 coverage issues noted previously, the $R_{TD,model}$ - MY time series in Figure 2i demonstrates
344 the same solar cycle period variation in the average Martian bow shock position that was
345 indicated earlier by the extrapolation method (Figure 2a).

346 The observed large dispersion in Figures 1c and 2b-2h are most probably caused by
347 short-time scale external variations of the incident solar wind plasma such as dynamic
348 pressure, IMF direction (convection electric field influence and dawn to dusk asymmetry)
349 or Mach numbers, but also possibly due to intrinsic microscopic variations of the
350 collisionless shock structure even during steady external conditions (non-stationary
351 character). All these variations occur on an orbit-to-orbit basis and do not influence the
352 average bow shock location on a much larger time scale when considered statistically.

353 In summary, the average bow shock position at the Martian terminator is closer to Mars
354 at low solar activity (e.g., MY28-29) than it is during the higher solar activity of solar
355 maximum (MY31-32). Quantitatively, this is an $\sim0.17R_M$ (or $\sim7\%$) increase in the
356 terminator position between the low and high solar activity periods of solar cycle 23/24.

357   This 7% solar cycle variation (which could be larger for other more extreme solar cycles,
358   see next section) occurs in addition to the overall 11% variation throughout the Martian
359   year (Hall et al., 2016). We note that the 11% annual variation was obtained after
360   averaging over all levels of solar activities. Due to the non-uniformity of observations
361   across every season and every year, it is not possible to get a robust estimation of the
362   annual bow shock location at each MY. Nevertheless, we show for the first time with the
363   same dataset that both annual and solar cycle variations play major roles in the variation
364   of the bow shock average location at Mars on a long-term basis.

365   **4. Discussion**

366   This study has aimed to answer the long-standing question of whether the Martian bow
367   shock position varies over the period of a solar cycle. We have used the Hall et al., (2016)
368   Martian bow shock crossing list and extended it with a newly released dataset to give ~13
369   years of MEX observations of the Martian bow shock crossings over the period of 2004
370   and 2017. This period includes ~7 Martian years occurring over solar cycles 23 and 24.
371   By modelling the average bow shock surface from the entire dataset (Figure 1), and from
372   each Martian year of observations (Figure 2), we have been able to demonstrate the bow
373   shock position varying over the period of a Martian year (first reported by Hall et al.,
374   2016), and solar cycle. We have also demonstrated that the magnitude of both of these
375   spatial and temporal variations are similar in magnitude to those seen in the solar EUV
376   flux over the period of the solar cycle. This suggests that along with driving the annual
377   variability in the bow shock position (Hall et al 2016), the solar EUV flux could also be a
378   main driver of the solar cycle period variations.

379   Earlier studies of this topic did not converge on a clear consensus regarding the role of
380   the solar EUV or Mars season regarding bow shock position (e.g., Russell et al., 1992,
381   Trotignon et al., 1993 compared to Slavin et al., 1991, Vignes et al., 2000; 2002). This was
382   likely due to the previous studies being limited by low numbers of bow shock
383   observations that often had both low sampling coverage across space, and the entirety of
384   even a single MY (e.g., maximum of 450 by MGS mission over sub-MY period). This, and
385   the Hall et al., (2016) study have both demonstrated the importance of considering how
386   Mars' position through its orbit of the Sun can significantly impact the average location
387   of the bow shock position. Unfortunately, the solar cycle period covered by MEX consisted

388   of both the lowest minimum and maximum levels of the recent solar cycle history (e.g.

389   McComas et al., 2013). Therefore, we expect that the percentage variation between

390   minimum and maximum at previous solar cycles were larger, proportional to their EUV

391   fluxes. Trotignon et al., (1993) compared the Mars-2,3,5 (low activity, solar cycle 20) and

392   Phobos-2 (high activity, solar cycle 22) bow shock crossings (see Tables 1 and 2) and

393   reported a solar cycle period variability with a total variation of ~11% in position at the

394   terminator. This is similar to the 7% we report here (e.g., comparing models from MY32

395   as high activity, and MY28 as low activity, Figure 2c,g,i), which might be slightly lower

396   due to the general lower activity of solar cycle 23/24 as compared to preceding cycles.

397   Accordingly, one would expect the bow shock position closer to Mars during the very-low

398   minimum of solar cycles 23/24 than at previous solar minima because of a much lower

399   EUV-flux level. However, it is not possible to conclude anything in this respect because

400   the number of observations from former missions is not sufficient to make a proper

401   statistical comparison. We can only say that R_{TD} at minimum of solar cycle 20 and

402   maximum of solar cycle 22 are reasonably comparable to the MEX estimates of solar cycle

403   23/24 (see Table 2). In addition, previous missions have observed bow shock crossings

404   over different regions over Mars. Only the near-continuous MEX and MAVEN (since 2014)

405   observations are able to provide a more coherent sample to assess this issue, which will

406   be improved in the coming years when two continuous solar cycles will be sampled, and

407   in-situ solar wind and solar radiation observations will be available for several Martian

408   years.

409   The orbits belonging to single-spacecraft observations of the Martian bow shock can

410   impact the results of studies such as this in two main ways. If the spacecraft has an orbital

411   apoapsis below the bow shock, it will simply not be observed. Similarly, if any

412   hemispherical asymmetries exist in the bow shock's location about Mars (e.g., Hall et al.,

413   2016), and a single spacecraft observes the bow shock in these hemispheres by different

414   amounts, a bias can quickly develop. Although this is undoubtedly a source of error, we

415   expect it to impact the results by a very small amount when compared to the whole MEX

416   dataset.

417   While the limitations of the earlier studies can explain the differences to our newfound

418   understanding reported here, recent attempts at theoretically modelling of the entire

419   Martian plasma system during differing levels of solar activity have also reported no

420   obvious solar cycle variations in the Martian bow shock position (e.g., Modolo et al., 2005;

421   2006; 2016). Here we only comment that this difference is surprising and that future

422   work should attempt to seek out why theoretical modelling attempts show no obvious

423   solar cycle variability.

424   In Figure 2a of Section 3, we noted how the standardized solar EUV flux (extrapolated to

425   Mars) and extrapolated bow shock terminator distance over the period of the solar cycle

426   both varied by similar extents over the Martian year and over the solar cycle periods.

427   Consequently, we agree with the mechanisms proposed by the Hall et al., (2016) study

428   where varying levels of solar EUV flux can modulate the way the solar wind interacts with

429   the Martian exosphere (exospheric ion pick-up) and ionosphere (enhanced ionization

430   and thermal pressure), resulting in a change in location of the bow shock position.

431   However, we noted in Section 3 that the extrapolated bow shock terminator distance

432   peaks more during perihelion than the solar EUV flux does during the same period (see

433   Figure 2a blue and red profiles). While we have no direct explanation for this, it could be

434   related to other more energetic radiation, such as the soft X-ray background irradiance

435   flux which ionized the ionosphere below the main peak. This is a clear future study line

436   to be done with MAVEN and MEX conjoined observations. In addition, another possible

437   explanation could reside in an annual (MY) variability in the average solar wind

438   magnetosonic Mach number at Mars.

439   Edberg et al., (2010) provided preliminary evidence that the Martian bow shock

440   terminator distance is linearly anti-correlated to the magnetosonic Mach number.

441   According to the Edberg et al., (2010) study, the expected lower average Mach number

442   during Mars' perihelion (c.f. aphelion) could drive the bow shock further from the planet

443   than what the solar EUV can do alone. This could explain the higher peaking of R_{TD} around

444   perihelion (compared to the solar EUV) noted here in our results (Figure 2a). This agrees

445   with the recent MAVEN results that have found that at the terminator distance, the bow

446   shock position moves around $0.2\ R_M$ closer to the planet during high magnetosonic Mach

447   number time periods, being 2.41-2.66 R_M (high-low Mach number) over the North pole

448   and 2.53-2.83 R_M over the South (Gruesbeck et al., 2018). Moreover, the magnetosonic

449   Mach number also anti-correlated with the solar cycle. Extrapolating once again from the

450   Edberg et al., (2009b) results, an on average lower Mach number at solar maximum

451   should result in the Martian bow shock being on average further away from the planet,

452   giving a similar effect on the bow shock position as described above at Mars perihelion.

453   While a MY filtered EUV profile is not shown in Figure 2, we have checked and found that

454   the 687-day filtered R'_{TD} during solar maximum does exceed the solar EUV flux filtered

455   to the same period, matching our observations at perihelion. Thus, the impact of the

456   magnetospheric Mach number on the average bow shock position with solar cycle is likely an

457   important driver that needs better parameterization. Moreover, as previously mentioned,

458   high magnetosonic Mach number also favors rapid oscillations of the bow shock front

459   location (non-stationarity). The role of the Mach number in this type of study could be

460   done in a future study together with MAVEN datasets. Currently, the MAVEN dataset

461   covers less than two Martian years and cannot be used today for a similar purpose.

462   However, one can take advantage of the MY32-33 overlapping of both missions and

463   compare similar datasets on both spacecraft, with the advantage that MAVEN can provide

464   all the necessary drivers.

465   While this study has provided clear evidence of the average Martian bow shock position

466   varying over both the Martian year and solar cycle, there are several routes that future

467   work could follow. Such topics include a full parameterization of statistical Martian bow

468   shock models (e.g., including dynamic pressure, IMF direction, Mach numbers, as well as

469   intrinsic microscopic variations of the shock structure) which may aid in explaining the

470   highly variable bow shock position on short time-scales. Also, a comparison with similar

471   (e.g., Venus, comets) and dissimilar (e.g., Earth, Mercury) plasma systems, as well as a

472   utilization of multi-spacecraft observations of the bow shock and inner Martian plasma

473   system (e.g., induced magnetosonic boundary and ionopause) in order to explain the

474   dynamics of the full plasma system as a whole. Finally, an assimilation of observational

475   datasets with theoretical models could be done to explain any differences.

476   **5. Conclusion**

477   In this paper we have used ~13 years of near-continuous observations of the Martian

478   bow shock by the Mars Express mission to report that its average position is sensitive to

479   solar activity, and thus varies over the solar cycle. We have provided evidence of this by

480   producing statistical models of the bow shock over long (entire bow shock crossing

481   dataset) and short (each of the 7 Martian years across solar cycle 23-24) time periods,

482   consequently using these results to estimate the extent of the variability. At the Martian

483   terminator, we have found that between a period of low and high solar activity, the

484   average Martian bow shock position increases by ~$0.17R_M$, or alternatively by an

485   increase in ~7%. This is similar in magnitude and in addition to the annual variability

486   noted by Hall et al., (2016), which reported an increase in the average Martian bow shock

487   position between Mars' aphelion and perihelion by ~$0.17R_M$ (~11%). Therefore, future

488   studies into the spatial variability of the Martian bow shock should take these aspects

489   into account, and with the continued support of both the MEX and MAVEN missions into

490   the coming years, future works will be able to provide a much more detailed

491   understanding of the variability reported here, and of the entire Martian plasma system.

511

512

References

Albee, A., F. D. Palluconi, and R. E. Arvidson (1998), Mars Global Surveyor Mission: Overview and Status, Science, 279 (5357), 1671-1672, doi: 403 10.1126/science.279.5357.1671.

Alexander C.J. and C.T. Russell, Solar cycle dependence of the location of the Venus bow shock, Geophys. Res. Lett., 12, 369, 1985.

Barabash, S., R. Lundin, H. Andersson, K. Brinkfeldt, A. Grigoriev, H. Gunell, M. Holmstrom, M. Yamauchi, K. Asamura, P. Bochsler, P. Wurz, R. Cerulli- Irelli, A. Mura, A. Milillo, M. Maggi, S. Orsini, a. J. Coates, D. R. Linder, D. O. Kataria, C. C. Curtis, K. C. Hsieh, B. R. Sandel, R. a. Frahm, J. R. Sharber, J. D. Winningham, M. Grande, E. Kallio, H. Koskinen, P. Riihela, W. Schmidt, T. S• ales, J. U. Kozyra, N. Krupp, J. Woch, S. Livi, J. G. Luhmann, S. McKenna- Lawlor, E. C. Roelof, D. J. Williams, J.-a. Sauvaud, A. Fedorov, and J.-J. Thocaven (2006), The Analyzer of Space Plasmas and Energetic Atoms (ASPERA-3) for the Mars Express Mission, Space Sci. Rev., 126 (1-4), 113-164, doi:10.1007/s11214-006-9124-8.

Chicarro, A., P. Martin, and R. Trautner (2004), The Mars Express mission: An overview, in Mars Express: The Scienti_c Payload, vol. SP-1240, edited by A. Wilson, pp. 3-13, ESA Publ. Div., Noordwijk, Netherlands.

Dolginov, S., and L. Zhuzgov (1991), The magnetic field and the magnetosphere of the planet Mars, Planet. Space Sci., 39 (11), 1493-1510, doi:10.1016/0032- 0633(91)90077- N.

Dolginov, S., Y. G. Yeroshenko, and L. N. Zhuzgov (1973), Magnetic field in the very close neighborhood of Mars according to data from the Mars 2 and Mars 3 spacecraft, J. Geophys. Res., 78 (22), 4779-4786, doi:10.1029/JA078i022p04779.

Dolginov, S., Y. G. Yeroshenko, and L. N. Zhuzgov (1976), The magnetic field of mars according to the data from the Mars 3 and Mars 5, J. Geophys. Res., 425 81 (19), 3353- 3362, doi:10.1029/JA081i019p03353.

539   Dryer, M., and G. R. Heckman (1967), Application of the hypersonic analog to the standing

540   shock of Mars, Sol. Phys., 2 (1), 112-124, doi:10.1007/BF00155897.

541   Edberg, N., D. A. Brain, M. Lester, S. W. H. Cowley, R. Modolo, M. Franz, and S. Barabash

542   (2009), Plasma boundary variability at Mars as observed by Mars Global Surveyor and

543   Mars Express, Ann. Geophys., 27 (9), 3537-3550, doi:431 10.5194/angeo-27-3537-2009.

544   Edberg, N., M. Lester, S. W. H. Cowley, D. A. Brain, M. Franz, and S. Barabash (2010),

545   Magnetosonic Mach number effect of the position of the bow shock at Mars in comparison

546   to Venus, J. Geophys. Res. Sp. Phys., 115 (A7), doi: 435 10.1029/2009JA014998.

547   Fushiki, T, (2011), Estimation of prediction error by using K-fold cross-validation, Stat.

548   Comput., 21 (2011), pp. 137-146, https://doi.org/10.1007/s11222-009-9153-8

549   Gruesbeck, J. R., Espley, J. R., Connerney, J. E. P., DiBraccio, G. A., Soobiah Y. I., D. Brain, et

550   al. (2018). The three-dimensional bow shock of Mars as observed by MAVEN. Journal of

551   Geophysical Research: Space Physics, 123, 4542–4555.

552   https://doi.org/10.1029/2018JA025366

553   Halekas, J. S., et al. (2017), Structure, dynamics, and seasonal variability of the Mars-solar

554   wind interaction: MAVEN Solar Wind Ion Analyzer in-flight performance and science

555   results, J. Geophys. Res. Space Physics, 122, 547–578, doi: 10.1002/2016JA023167.

556   Hall, B., M. Lester, B. Sanchez-Cano, J. D. Nichols, D. J. Andrews, N. J. T. Edberg, H. J.

557   Opgenoorth, M. Franz, M. Holmstrom, R. Ramstad, O. Witasse, M. Cartacci, A. Cicchetti, R.

558   Noschese, and R. Orosei (2016), Annual variations in the Martian bow shock location as

559   observed by the Mars Express mission, J. Geophys. Res. Sp. Phys., 121 (11), 11,474-

560   11,494, doi:10.1002/2016JA023316.

561   Hughes, I., and T. Hase (2010), Measurements and their Uncertainties, Oxford University

562   Press, Great Clarendon Street, Oxford OX2 6DP.

563 King, J., and N. E. Papitashvili (2005), Solar wind spatial scales in and comparisons of
564 hourly Wind and ACE plasma and magnetic _eld data, J. Geophys. Res. Sp. 445 Phys., 110
565 (A2), 1-9, doi:10.1029/2004JA010649.

566 Marov, M., and G. Petrov (1973), Investigations of Mars from the Soviet automatic stations
567 Mars 2 and 3, Icarus, 19 (2), 163-179, doi:10.1016/0019-1035(73)90120-6.

568 McComas, D. J., N. Angold, H. A. Elliott, G. Livadiotis, N. A. Schwadron, R. M. Skoug, and C.
569 W. Smith (2013), Weakest solar wind of the space age and the current "Mini" solar
570 maximum, Astrophys. J., 779, 2, doi: 10.1088/0004-637X/779/1/2.

571 Mazelle, C., et al. (2004), Bow shock and upstream phenomena at Mars, Space Sci. Rev.,
572 111(1/2), 115–181, doi:10.1023/B:SPAC.0000032717.98679.d0

573 Mendillo, M., P. Withers, D. Hinson, H. Rishbeth, and B. Reinisch (2006), Effects of solar
574 flares on the ionosphere of Mars, Science, 311, 1135–1138,
575 doi:10.1126/science.1122099.

576 Modolo, R., G. M. Chanteur, E. Dubinin, and A. P. Matthews (2005), Inuence of the solar
577 EUV ux on the Martian plasma environment, Ann. Geophys., 23 (2), 433-444,
578 doi:10.5194/angeo-23-433-2005.

579 Modolo, R., G. M. Chanteur, E. Dubinin, and A. P. Matthews (2006), Simulated solar wind
580 plasma interaction with the Martian exosphere: inuence of the solar EUV flux on the bow
581 shock and the magnetic pile-up boundary, Ann. Geophys., 24 (12), 3403-3410,
582 doi:10.5194/angeo-24-3403-2006.

583 Modolo, R., S. Hess, M. Mancini, F. Leblanc, J.-y. Chaufray, D. Brain, L. Leclercq, R. Esteban-
584 Hernandez, G. Chanteur, P. Weill, F. Gonzalez-Galindo, F. Forget, M. Yagi, and C. Mazelle
585 (2016), Mars-solar wind interaction: LatHyS, an improved parallel 3-D multispecies
586 hybrid model, J. Geophys. Res. Sp. Phys., pp.1-22, doi:10.1002/2015JA022324.

587 Riedler, W., D. Mohlmann, V. N. Oraevsky, K. Schwingenschuh, Y. Yeroshenko, J.
588 Rustenbach, O. Aydogar, G. Berghofer, H. Lichtenegger, M. Delva, G. Schelch, K. Pirsch, G.

589   Fremuth, M. Steller, H. Arnold, T. Raditsch, U. Auster, K.-H. Fornacon, H. J. Schenk, H.

590   Michaelis, U. Motschmann, T. Roatsch, K. Sauer, R. Schro• ter, J. Kurths, D. Lenners, J.

591   Linthe, V. Kobzev, V. Styashkin, J. Achache, J. Slavin, J. G. Luhmann, and C. T. Russell (1989),

592   Magnetic fields near Mars: first results, Nature, (6243), 604-607, doi:10.1038/341604a0.

593   Russell, C. (1977), On the relative locations of the bow shocks of the terrestrial planets,

594   Geophys. Res. Lett., 4 (10), 387-390, doi:10.1029/GL004i010p00387.

595   Russell, C. (1980), Planetary magnetism, Rev. Geophys., 18 (1), 77, doi:

596   10.1029/RG018i001p00077.

597   Russell, C., M. Ong, J. Luhmann, K. Schwingenschuh, W. Riedler, and Y. Yeroshenko (1992),

598   Bow shocks and magnetotails of Venus and Mars: A comparison, Adv. Sp. Res., 12 (9), 163-

599   167, doi:10.1016/0273-1177(92)90329-V.

600   Sánchez-Cano, B., M. Lester, O. Witasse, S. E. Milan, B. E. S. Hall, P.-L. Blelly, S. M. Radicella,

601   and D. D. Morgan (2015), Evidence of scale height variations in the Martian ionosphere

602   over the solar cycle, J. Geophys. Res. Space Physics, 120, doi:10.1002/2015JA021949.

603   Sánchez-Cano, B., et al. (2016), Solar cycle variations in the ionosphere of Mars as seen

604   by multiple Mars Express data sets, J. Geophys. Res. Space Physics, 121,

605   doi:10.1002/2015JA022281.

606   Sánchez-Cano, B., Lester, M., Witasse, O., Blelly, P.-L., Indurain, M., Cartacci, M., et al.

607   (2018). Spatial, seasonal, and solar cycle variations of the Martian total electron content

608   (TEC): Is the TEC a good tracer for atmospheric cycles? Journal of Geophysical Research:

609   Planets, 123, 1746–1759. https://doi.org/10.1029/2018JE005626

610   Slavin, J., and R. E. Holzer (1982), The solar wind interaction with Mars revisited, J.

611   Geophys. Res., 87 (B12), 10,285, doi:10.1029/JB087iB12p10285.

612   Slavin, J., K. Schwingenschuh, W. Riedler, E. Eroshenko, and Y. Yeroshenko (1991), The

613   solar wind interaction with Mars: Mariner 4, Mars 2, Mars 3, Mars 5, and Phobos 2

614   observations of bow shock position and shape, J. Geophys. Res., 96 (A7), 11,235,

615   doi:10.1029/91JA00439.

616 Smith, E. (1969), Planetary Magnetic Field Experiments, in Advanced Space Experiments,
617 edited by O. L. Ti_any and E. M. Zaitze_, pp. 103-130, American Astronautical Society,
618 Tarzan, Calif.

619 Smith, E., L. Davis, P. J. Coleman, and D. E. Jones (1965), Magnetic field measurements near
620 mars, Science, 149 (3689), 1241-1242, doi:10.1126/science.149.3689.1241.

621 Trotignon, J., R. Grard, and A. Skalsky (1993), Position and shape of the Martian bow
622 shock: the Phobos 2 plasma wave system observations, Planet. Space Sci.,41 (3), 189-198,
623 doi:10.1016/0032-0633(93)90058-A.

624 Vignes, D., C. Mazelle, H. Rme, M. H. Acuna, J. E. P. Connerney, R. P. Lin, D. L. Mitchell, P.
625 Cloutier, D. H. Crider, and N. F. Ness (2000), The solar wind interaction with Mars:
626 Locations and shapes of the bow shock and the magnetic pile-up boundary from the
627 observations of the MAG/ER Experiment onboard Mars Global Surveyor, Geophys. Res.
628 Lett., 27 (1), 49-52, doi:10.1029/1999GL010703.

629 Vignes, D., M. H. Acuna, J. E. P. Connerney, D. H. Crider, H. Reme, and C. Mazelle (2002),
630 Factors controlling the location of the Bow Shock at Mars, Geophys. Res. Lett., 29 (9),
631 doi:10.1029/2001GL014513.

632 Woods, T. N., S. M. Bailey, F. G. Eparvier, G. M. Lawrence, J. Lean, W. E. McClintock, R. G.
633 Roble, G. J. Rottman, S. C. Solomon, W. K. Tobiska, G. J. Ucker, and O. R. White (1998),
634 TIMED solar euv experiment, doi:10.1117/12.330255.

635 Yamauchi, M., T. Hara, R. Lundin, E. Dubinin, A. Fedorov, J.-A. Sauvaud, R. Frahm, R.
636 Ramstad, Y. Futaana, M. Holmstrom, and S. Barabash (2015), Seasonal variation of
637 Martian pick-up ions: Evidence of breathing exosphere, Planet. Space Sci., 119, 54-61,
638 doi:10.1016/j.pss.2015.09.013.

639

640

641 **Table 1:** Time periods of missions to Mars that obtained bow shock information

Mission	Type	Date	Solar Cycle Phase (and number of Solar Cycle)	Ls
Mariner 4	Fly-by	1965-07-15	MIN(20)	143°
Mars 2	Orbiter	1971-11-27 to 1972-08-22	LATE MAX(20)	300°–73° (133° total)
Mars 3	Orbiter	1971-12-02 to 1972-08-22	LATE MAX(20)	303°–73° (130° total)
Mars 5	Orbiter	1974-02-12 to 1974-02-28	END(20), near MIN(21)	6°–14° (8° total)
Phobos 2	Orbiter	1989-01-29 to 1989-03-27	near MAX(22)	350°–19° (29° total)
MGS	Orbiter	1997-09-12 to 1998-08-29	LATE MIN/EARLY MAX (23)	180°–22° (202° total)
MEX	Orbiter	2003-12-25 to Present	LATE MAX (23)/ MIN and MAX(24)	ALL
MAVEN	Orbiter	2014-09-24 to Present	MIN and MAX (24)	ALL

642

643

644

645

646

647

648

649

650

651

652

653

654

655

656

657 **Table 2:** Previous studies of solar cycle variation in the bow shock

Authors	Mission	N_{Cross} [#]	SSN [#]	$F_{10.7}$ [sfu]	I_{EUV} [mW m^{-2}]	R_{SS} [R_M]	R_{TD} [R_M]	Solar Cycle Variation?
Slavin et al. [1991]	Mariner-Mars	24	59	---	---	1.55	2.29	NO
	Phobos-2	94	141	---	---	1.58	2.57	
Trotignon et al. [1993]	Mars-2,3,5	14	59	---	---	1.50	2.36	YES
	Phobos-2	126	141	---	---	1.57	2.63	
Vignes et al. [2000, 2002]	Phobos-2	94/126	140-180	---	---	1.58/1.57	2.57/2.63	NO
	MGS	450	30-90	---	---	1.64/1.67	2.62/2.56	
Modolo et al. [2005, 2006]	Hybrid Simulations	---	---	---	MIN	1.72	2.73	NO
	Hybrid Simulations	---	---	---	MAX	1.76	2.64	
Modolo et al. [2016]	Hybrid Simulations	---	---	---	MIN	1.5	---	NO
	Hybrid Simulations	---	---	---	MAX	1.45	---	
This Study	MEX MIN:24	5582	0-52 Avg~10	67-96 Avg~75	3.12-5.27 Avg~3.95	1.62	2.38	YES
	MEX MAX:24	5824	41-151 Avg~90	93-166 Avg~130	3.79-7.16 Avg~5.07	1.72	2.52	

658

659

660

661

662

663

664

665 **Table 3.** Best Fit Values of Conic Section Fitted to Different Periods of MEX Bow Shock

666 Observations

Martian Year(s)	Observations [#]	R^2	x_0 [RM]	L [RM]	ϵ	$R_{TD, model}$
ALL	13585	0.89	0.76	1.802 ± 2.10^{-3}	0.998 ± 3.10^{-3}	2.445 ± 3.10^{-3}
27	408	0.92	0.57	1.924 ± 12.10^{-3}	0.978 ± 16.10^{-3}	2.415 ± 12.10^{-3}
28	1874	0.90	0.78	1.678 ± 5.10^{-3}	1.006 ± 8.10^{-3}	2.336 ± 6.10^{-3}
29	2140	0.94	0.79	1.685 ± 5.10^{-3}	1.041 ± 7.10^{-3}	2.380 ± 5.10^{-3}
30	2411	0.92	0.70	1.863 ± 5.10^{-3}	0.997 ± 7.10^{-3}	2.463 ± 6.10^{-3}
31	2680	0.87	0.80	1.825 ± 5.10^{-3}	0.971 ± 8.10^{-3}	2.476 ± 6.10^{-3}
32	2578	0.79	0.90	1.791 ± 6.10^{-3}	0.970 ± 10.10^{-3}	2.507 ± 8.10^{-3}
33	1494	0.88	0.78	1.782 ± 7.10^{-3}	0.985 ± 10.10^{-3}	2.428 ± 8.10^{-3}

667

668

669

670
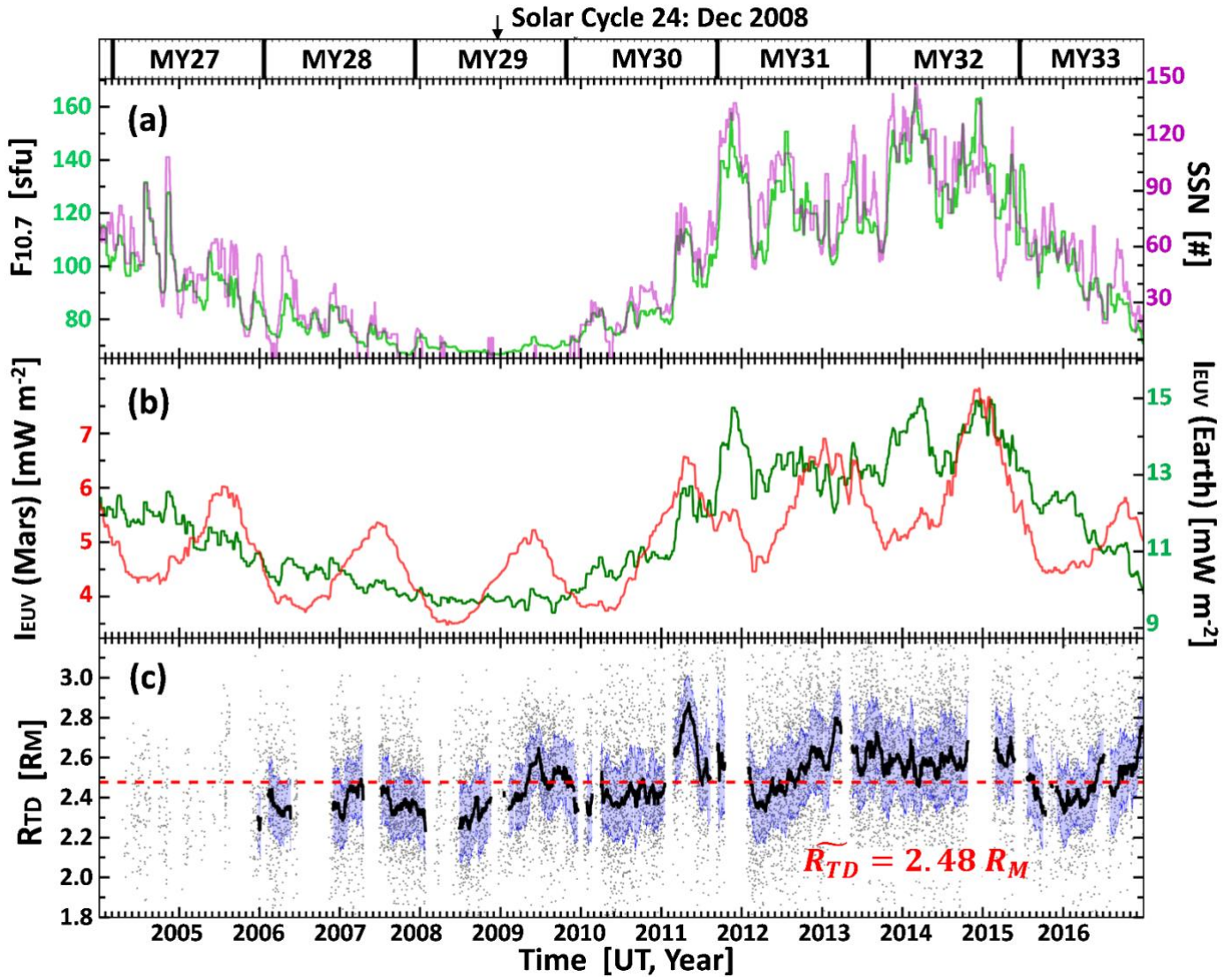
Figure 1: Time series of solar parameters and Martian bow shock terminator distance. Panel (a) OMNI-2 10.7cm solar radio flux, F10:7 (left, green), and Sun Spot Number, SSN (right, purple). (b) TIMED-SEE solar EUV flux (IEUV) at Earth (right, green) and extrapolated to Mars (left, red). (c) Extended HALL16 bow shock extrapolated terminator distance dataset. All time-series shown for period of 2004 -2017 with the corresponding Martian Years (MY) shown atop panel (a). See text in Sections 2 and 3 for details.
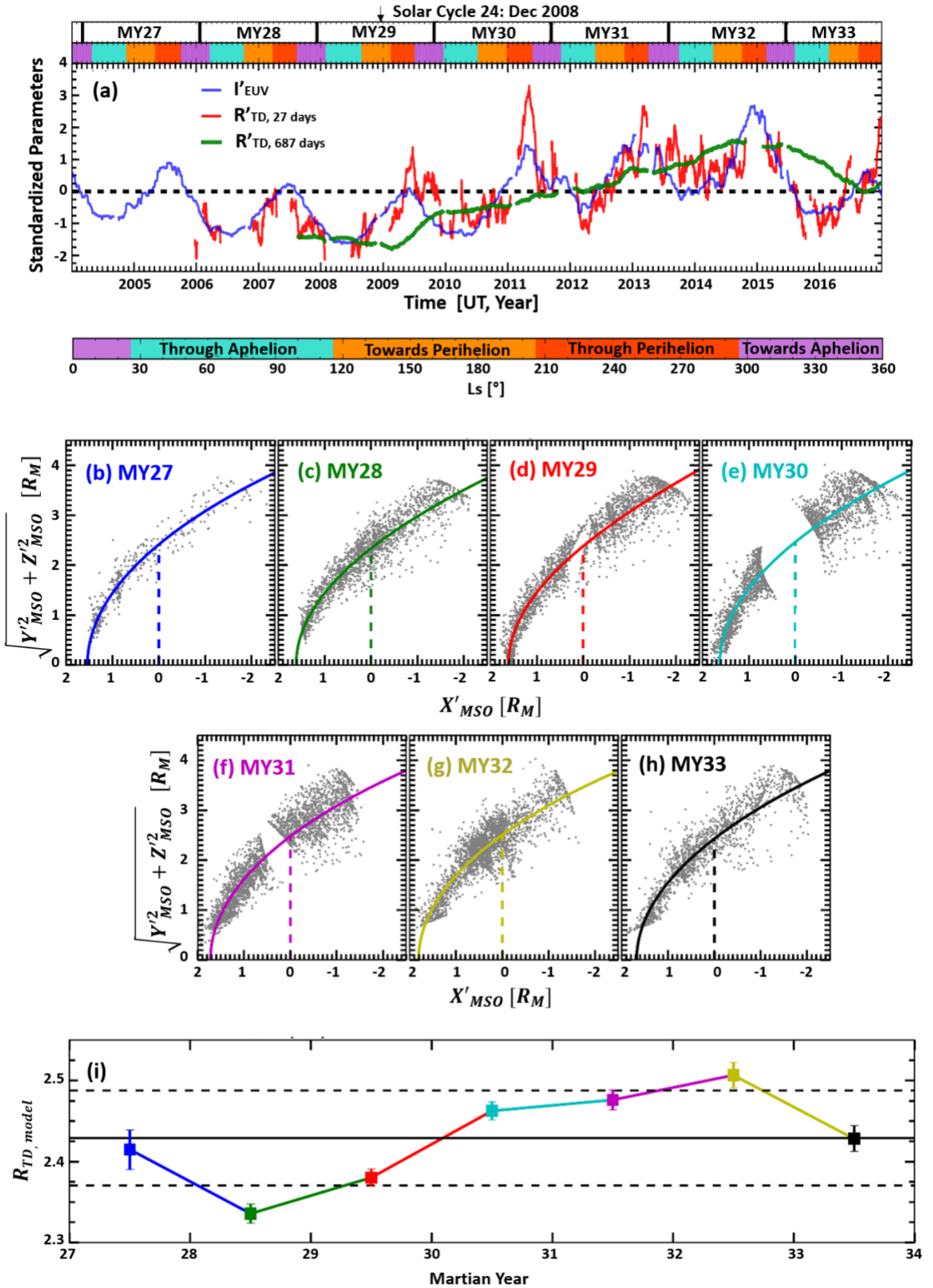
682   **Figure 2:** Panel (a) Median-filtered (27-day: blue) TIMED-SEE solar EUV flux (I'_{EUV}) at

683   Mars, and median filtered (27-day: red, 687-day/MY: red) extended HALL16 bow shock

684   extrapolated terminator distance dataset, both in terms of standardized units for direct

685   comparison. Panels (b-h) MEX bow shock crossings in solar wind aberrated axisymmetric

686   MSO coordinate frame. Statistical model fits to data shown by colored curves. Panel (i)

687   MY time-series of model bow shock terminator distances for each MY shown in panels b-

688   h. See text in Section 3 for details.